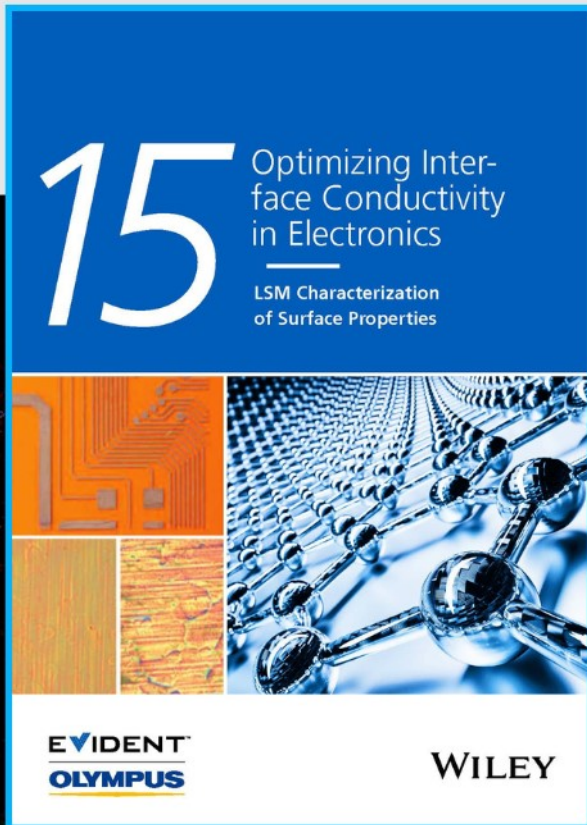




Optimizing Interface Conductivity in Electronics



The latest eBook from
Advanced Optical Metrology.
Download for free.

Surface roughness is a key parameter for judging the performance of a given material's surface quality for its electronic application. A powerful tool to measure surface roughness is 3D laser scanning confocal microscopy (LSM), which will allow you to assess roughness and compare production and finishing methods, and improve these methods based on mathematical models.

Focus on creating high-conductivity electronic devices with minimal power loss using laser scanning microscopy is an effective tool to discern a variety of roughness parameters.

EVIDENT
OLYMPUS

WILEY

SnP₂O₇ Covered Carbon Nanosheets as a Long-Life and High-Rate Anode Material for Sodium-Ion Batteries

Jun Pan, Shulin Chen, Dapeng Zhang, Xuena Xu, Yuanwei Sun, Fang Tian, Peng Gao, and Jian Yang*

SnP₂O₇ attached to reduced graphene oxide (rGO) is synthesized by a solvothermal reaction, followed by a mild annealing in Ar/H₂. As an anode material for sodium-ion batteries, this composite is associated with the conversion reaction between Sn and SnP₂O₇ and the alloy reaction between Sn and Na_xSn, as evidenced by ex situ techniques, such as high-resolution transmission electron microscope images, selected area electron diffraction patterns, and X-ray diffraction patterns. The close contact between SnP₂O₇ and rGO facilitates the charge transfer upon cycling and benefits the preservation of SnP₂O₇ on rGO even after pulverization. Therefore, this composite exhibits an extraordinary cycling stability. 99% of the initial capacity is remained after 200 cycles at 0.2 A g⁻¹ and also 99% is kept after 1000 cycles at 1.0 A g⁻¹. The similar results are also observed in full cells. Quantitative kinetic analysis confirms that sodium storage in this composite is governed by pseudocapacitance, especially at high rates. These results indicate the promising potential of metal pyrophosphates in sodium-ion batteries.

portable electronics and electrical vehicles.^[1–6] However, the low abundance of lithium in earth limits their applications in massive energy storage.^[7–10] Thus, sodium-ion batteries (SIBs) revive as an alternative of LIBs, due to high natural abundance and low cost of Na reserves as compared to Li.^[11,12] Compared to LIBs, the large ion radius of Na⁺ greatly increases the diffusion barrier and retards the sodiation/desodiation kinetics in conventional anode materials,^[13] such as carbon materials, transitional metal oxides/sulfides, and so forth. Moreover, the low voltage plateau of carbon readily leads to the formation of sodium dendrites and causes severe safety concerns.^[14,15] Metal oxides/sulfides suffer from enormous volume expansion and intermediate dissolution, resulting in poor cycling stability and capacity retention.^[16–18]

1. Introduction

Lithium-ion batteries (LIBs), as an efficient energy storage device, have achieved great successes in many fields, such as

The exploration of new electrode materials is highly desirable for SIBs.

Alloy-type anode materials in SIBs exhibit high theoretical capacities and moderate working voltages.^[19–21] Compared to toxic Sb and inflammable P, Sn-based materials are environmental friendliness and low cost.^[22] In a number of Sn-based materials, metallic Sn has a high theoretical capacity about 847 mA h g⁻¹ and also faces to a huge volume variation upon cycling.^[23] In order to address this issue, Sn is fabricated as elaborate nanostructures,^[24] carbon composites,^[25] or other compounds such as SnO₂, SnS₂, and SnSe.^[26–28] Although these strategies improve the electrochemical performances to some extent, they are still far away from being satisfactory. Recently, Sn₂P₂O₇ was evaluated as an anode material in SIBs with the focus on the advantages of amorphous Sn₂P₂O₇ over its crystalline counterpart.^[29] The capacity retention of amorphous Sn₂P₂O₇/reduced graphene oxide (rGO) was ≈80% after 100 cycles at 50 mA g⁻¹, much better than ≈40% of crystalline Sn₂P₂O₇/rGO. However, no matter amorphous or crystalline Sn₂P₂O₇, the electrochemical reactions upon the cycling, especially those occurred during the charge processes, were not evidenced.

Here, crystalline SnP₂O₇/rGO is used to demonstrate that crystalline phase can also show excellent performances. After 200 cycles at 0.2 A g⁻¹, the capacity of SnP₂O₇/rGO is maintained at 99%, much better than the previous result. The similar result is also observed in the long-term cycling up to 1000 cycles or at a high rate up to 8 A g⁻¹. The close interaction of rGO and

J. Pan, D. P. Zhang, X. N. Xu, F. Tian, Prof. J. Yang
Key Laboratory of Colloid and Interface Chemistry
Ministry of Education
School of Chemistry and Chemical Engineering
Shandong University
Jinan 250100, P. R. China
E-mail: yangjian@sdu.edu.cn

S. L. Chen, Y. W. Sun, Prof. P. Gao
International Center for Quantum Materials
and Electron Microscopy Laboratory
School of Physics
Peking University
Beijing 100871, P. R. China

S. L. Chen
State Key Laboratory of Advanced Welding and Joining
Harbin Institute of Technology
Harbin 150001, P. R. China
Prof. P. Gao
Collaborative Innovation Center of Quantum Matter
Beijing 100871, P. R. China

 The ORCID identification number(s) for the author(s) of this article can be found under <https://doi.org/10.1002/adfm.201804672>.

DOI: 10.1002/adfm.201804672

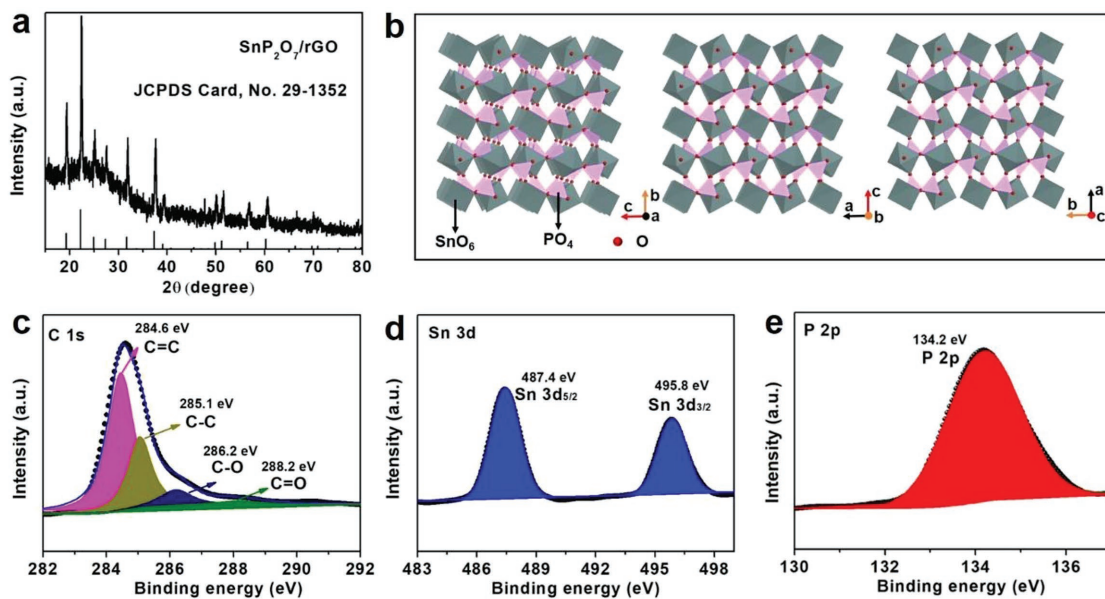


Figure 1. Crystal structure and component characterization of SnP₂O₇/rGO. a) XRD pattern. b) Crystal structure in different directions. XPS spectra of SnP₂O₇/rGO, c) C 1s, d) Sn 3d, and e) P 2p.

SnP₂O₇ promotes the charge transfer during the discharge/charge processes and benefits the adhesion of SnP₂O₇ to rGO, leading to a superior cycling stability. High-resolution transmission electron microscope (HRTEM) images, selected-area electron diffraction (SAED) patterns, and X-ray diffraction (XRD) patterns are employed to disclose the underlying electrochemical reactions, especially those happened to the charging process. To our knowledge, it is the first time to evidence these reactions.

2. Results and Discussion

SnP₂O₇/rGO is synthesized by a simple solvothermal reaction between SnCl₄·5H₂O and NH₄H₂PO₄ in the presence of GO, followed by a mild annealing in Ar/H₂ at 550 °C. The obtained powders were characterized by the XRD pattern first. As shown in **Figure 1a**, all the diffractions could be indexed as those from cubic-phase SnP₂O₇ (joint committee on powder diffraction standards (JCPDS) Card, No. 29-1352) composed by corner-sharing SnO₆ octahedra and PO₄ tetrahedra linked together to form P₂O₇ units (the inset of **Figure 1b**).^[30] However, P—O—P linkages in P₂O₇ units are partially or completely bent at low temperature, resulting in a pseudo-cubic structure with a tripled (3 × 3 × 3) unit cell. The broad bulge over 20°–30° in the XRD pattern indicates carbon materials in the powders, well consistent with rGO in SnP₂O₇/rGO. This result is further supported by Raman spectrum, X-ray photoelectron spectra (XPS), and TEM techniques. As displayed in Raman spectrum (**Figure S1**, Supporting Information), there are two peaks at 1345 and 1580 cm⁻¹ resulted from disordered carbon (D band) and graphitic carbon (G band) respectively. The high ratio of D/G bands indicates high-density structure defects and lattice distortion, which may be ascribed to numerous oxygenous groups in rGO. To confirm this point, high-resolution spectrum of C 1s was fitted by multiple peaks (**Figure 1c**), which are 284.6 eV from sp²-bonded

C=C, 285.1 eV from sp²-bonded C—C, 286.2 eV from C—O, and 288.2 eV from C=O.^[31] These functional groups make SnP₂O₇, or intermediates like Sn or Na₁₅Sn₄ to adhere on rGO firmly, thus reducing the interface impedance and inhibiting their separation from rGO.^[32] Meanwhile, the characteristic peaks of Sn, P, and O are also observed in the survey spectrum (**Figure S2**, Supporting Information). The high-resolution spectrum of Sn 3d (**Figure 1d**) exhibits two peaks at 487.4 and 495.8 eV from Sn 3d_{5/2} and Sn 3d_{3/2} of Sn⁴⁺ in SnP₂O₇.^[33] The strong peak at 134.2 eV can be assigned to P 2p of PO₄ tetrahedra (**Figure 1e**).^[34] On the basis of these results, the powders are marked as SnP₂O₇/rGO in short from now on. The ratio of SnP₂O₇ to rGO in the composite can be estimated by thermogravimetric analysis (TGA) (**Figure S3**, Supporting Information). The weight loss over 500–600 °C in air is due to the removal of rGO (**Figure S4**, Supporting Information). Therefore, the content of rGO in the composite is calculated as 16.8 wt%. N₂ sorption isotherms of SnP₂O₇/rGO (**Figure S5**, Supporting Information) show a small hysteresis loop in the *p/p*₀ range of 0.5–1.0, suggesting the formation of a mesoporous structure. The specific surface area and average pore size computed by Brunauer–Emmett–Teller model are 42.58 m² g⁻¹ and 20–40 nm, respectively.

The overall morphology, crystal structure, and component distribution of SnP₂O₇/rGO were characterized by scanning electron microscope (SEM) and TEM techniques. Low-magnification SEM image (**Figure 2a**) reveals that SnP₂O₇ has been uniformly embedded in rGO. The close-up check on a randomly selected area (**Figure 2b**) discloses a large number of layer-like structures in SnP₂O₇/rGO. These layer structures likely inherit from rGO and serve as a scaffold for the growth of SnP₂O₇. At the same time, these layers stack together and form a 3D network, leaving a lot of voids between neighboring layers. The voids enable the electrolyte fast infiltration, promote the electrode/electrolyte contact, and reduce the electrode polarization. Meanwhile, the voids also allow SnP₂O₇/

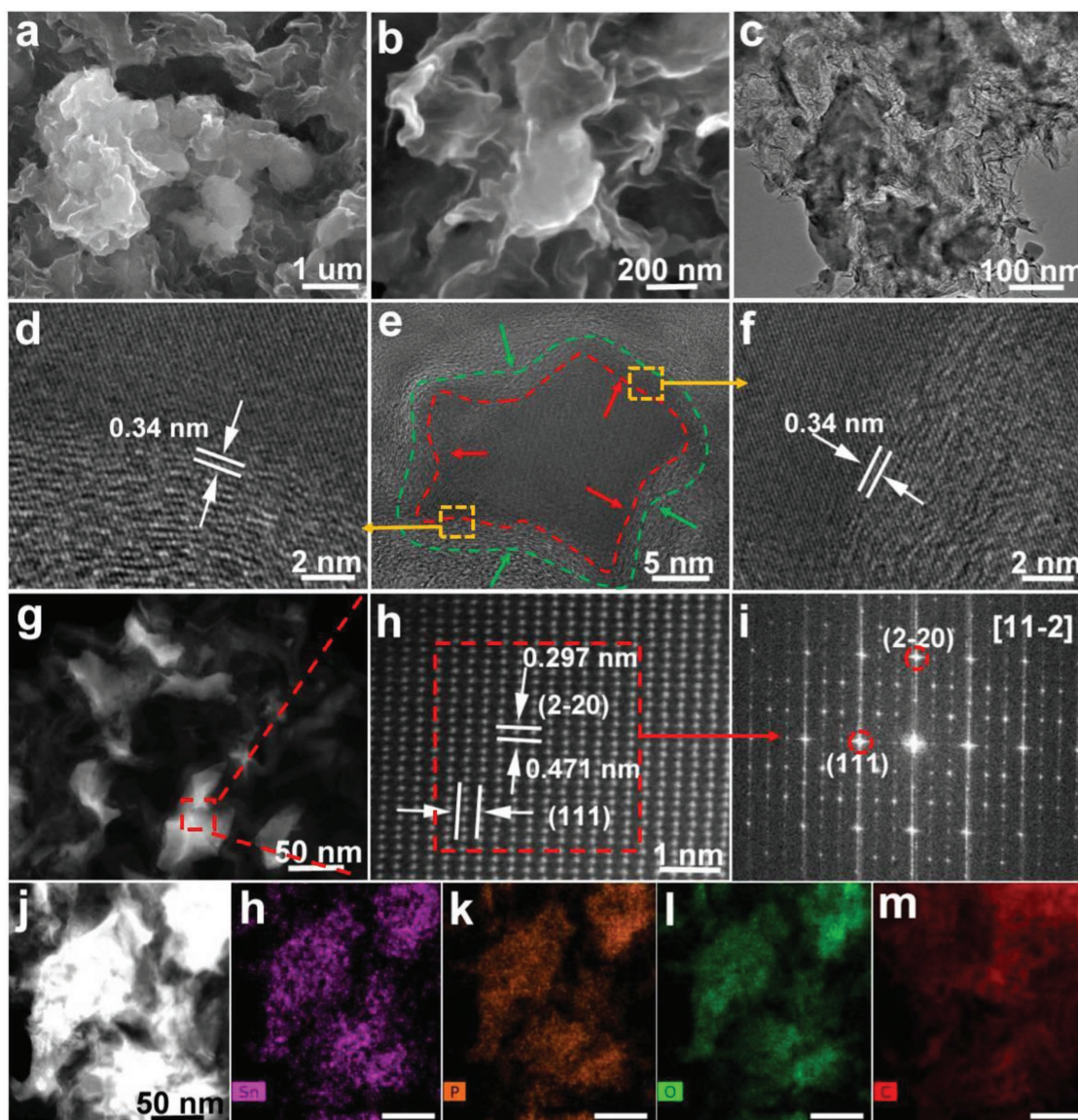


Figure 2. Morphology and components of $\text{SnP}_2\text{O}_7/\text{rGO}$. a,b) FESEM images, c) TEM image, d–f) HRTEM images, g) HAADF-STEM image, h) atom-resolution HRTEM images, i) FFT pattern, j) HAADF-STEM image, and k–n) elemental maps of Sn, P, O, and C.

rGO to accommodate the volume change upon cycling and then maintain a stable structure. More importantly, the layer structure with their thickness on the order of nanometers greatly shortens the diffusion distance of charge transportation during cycles, especially in the direction normal to the basal plane. SEM and TEM images of $\text{SnP}_2\text{O}_7/\text{rGO}$ (Figure 2b,c) show that rGO is highly crimped, which can effectively lower the nucleation barrier for SnP_2O_7 and enhance the adhesion of SnP_2O_7 to rGO. SnP_2O_7 on rGO is composed of irregular particles with their sizes on the order of several hundreds of nanometers. These particles are firmly attached to rGO, since no separated SnP_2O_7 and rGO are observed in TEM images. HRTEM image at the interface of SnP_2O_7 and rGO indicates that SnP_2O_7 and rGO are closely attached to each other at the interface (Figure 2d–f), confirming the strong adhesion between them. It has been well-documented that the decent

adhesion between carbon and active materials could effectively reduce the interface impedance and restrain the particle aggregation upon cycling.^[35] High-angle annular dark-field scanning TEM (HAADF-STEM) image (Figure 2g) provides us another way to identify the spatial distribution of SnP_2O_7 and rGO. The arrangement of Sn atoms is atomically resolved along the [11-2] zone axis (Figure 2h) judging from the corresponding fast Fourier transform (FFT) pattern (Figure 2i). Note that O and P atoms are not well identified due to their low atomic masses. Besides, some superstructure spots are observed in Figure 2i, compared to that of the simulated electron diffraction (Figure S6, Supporting Information), which is likely due to the distortion of the Sn atoms. Element mapping can give a scenario on the distribution of different components.^[36] Energy dispersive X-ray spectrum (EDS) was measured to confirm the existences of Sn, P, O, and C in the composite

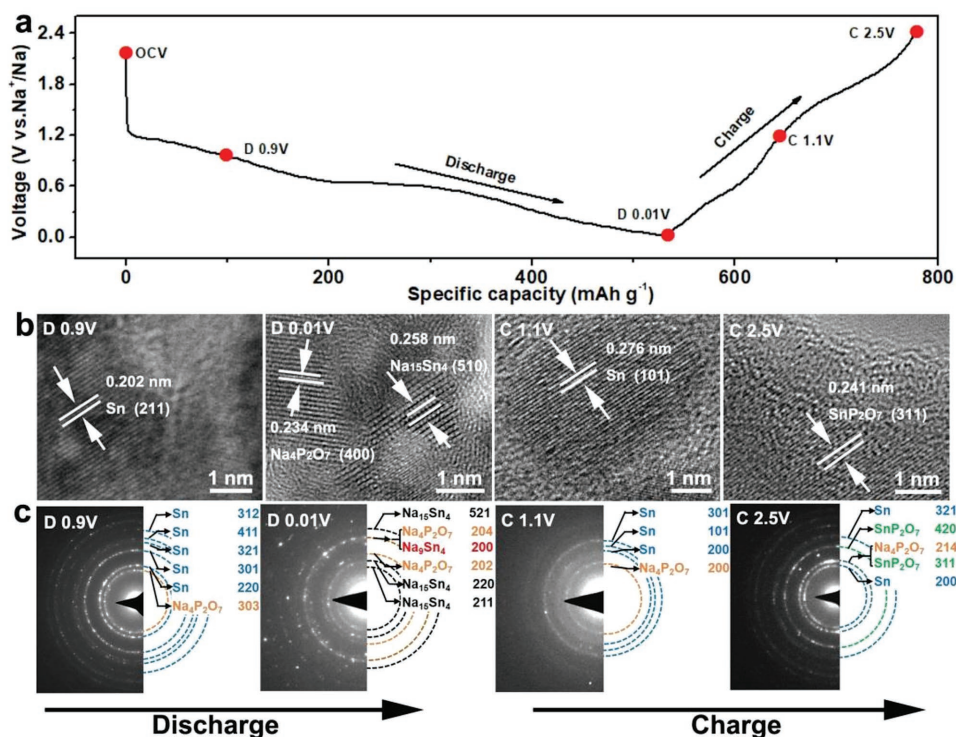


Figure 3. Electrochemical reactions during the discharge/charge processes of $\text{SnP}_2\text{O}_7/\text{rGO}$. a) Discharge/charge profiles of $\text{SnP}_2\text{O}_7/\text{rGO}$ at the first cycle. b,c) Ex situ HRTEM images and SAED patterns at the first cycle.

(Figure S7, Supporting Information). Then, the signals of Sn (purple), P (orange), O (green), and C (red) were collected individually to identify their location in the composite. As shown in Figure 2j–n, Sn, P, and O present a similar distribution pattern, consistent with the formation of SnP_2O_7 . The case of carbon is different. Its signal covers a larger area than those of Sn, P, and O, consistent with its role as a scaffold for the deposition of SnP_2O_7 .

In order to clarify the electrochemical reactions on $\text{SnP}_2\text{O}_7/\text{rGO}$ during the discharge/charge processes, ex situ characterization techniques, such as XRD patterns, HRTEM images and SAED patterns were measured for the intermediates at different states of discharge/charge. Unfortunately, ex situ XRD patterns do not offer useful clues to identify these electrochemical reactions, due to the absence of unambiguous diffraction peaks (Figure S8, Supporting Information). This phenomenon always happens to electrode materials based on conversion/alloying reactions.^[37] In this context, ex situ SAED patterns and HRTEM images were used to investigate the intermediates, because both of them are powerful tools to identify small and poorly crystallized particles. As shown in Figure 3a, there is a voltage slope over 1.2–0.6 V, resulting in a capacity of $\approx 190 \text{ mA h g}^{-1}$ (Figure S9, Supporting Information). Here, the total mass of SnP_2O_7 and rGO is included to compute the specific capacity. This Na-ion uptake could be attributed to the reduction of Sn (IV) to Sn (0), as confirmed by HRTEM images and SAED patterns (D 0.9 V in Figure 3b,c). However, the capacity is less than the theoretical capacity (366 mA h g^{-1}) calculated from the full conversion reactions, suggesting the incomplete reduction of SnP_2O_7 . After that, the discharge profile proceeds with

a pronounced voltage plateau at 0.6 V, followed by a long slope to 0.01 V. This process is related to the alloying of metallic Sn (D 0.01 V in Figure 3b,c), the intercalation of Na ions into carbon, the formation of a solid-electrolyte interphase (SEI) film, and so on. As the electrode is charged back to 1.1 V, metallic Sn appears again in HRTEM images and SAED patterns (C 1.1 V in Figure 3b,c), confirming the reversible dealloying of Sn. However, only a specific capacity of 100 mA h g^{-1} is released, much smaller than the counterpart at the first discharge. The similar result is also observed for the charge behavior over 1.1–2.5 V. What is important is that SnP_2O_7 is formed again at 2.5 V as revealed by HRTEM images and SAED patterns (C 2.5 V in Figure 3b,c), despite this electrochemical oxidation is partially reversible. Actually, the repeated breaking and formation of Sn–O in phosphates has been documented in lithium ion batteries.^[38]

Figure 4a shows the cyclic voltammograms (CVs) of $\text{SnP}_2\text{O}_7/\text{rGO}$ during the first three cycles in the range of 0.01–2.5 V at a scan rate of 0.1 mV s^{-1} . In the first discharging, the broad peak at 0.9 V is due to the reduction of SnP_2O_7 to metallic Sn, the formation of a SEI film, the alloying of Sn–Na, and so on.^[39] After that, it follows by a peak close to 0.01 V, which could be attributed to the intercalation of Na ions into carbon. Then, as the electrode is charged back to 2.5 V, Na ions are extracted from carbon and Na_xSn , resulting in the two peaks at 0.25 and 0.6 V. The peak at 1.8 V is likely nested in the oxidation of Sn to SnP_2O_7 ,^[40] consistent with what observed in SAED and HRTEM images. In the second cycle, the cathodic peak corresponding to the reduction of SnP_2O_7 to metallic Sn moves to 1.5 V, indicating the reduced polarization for this reaction.

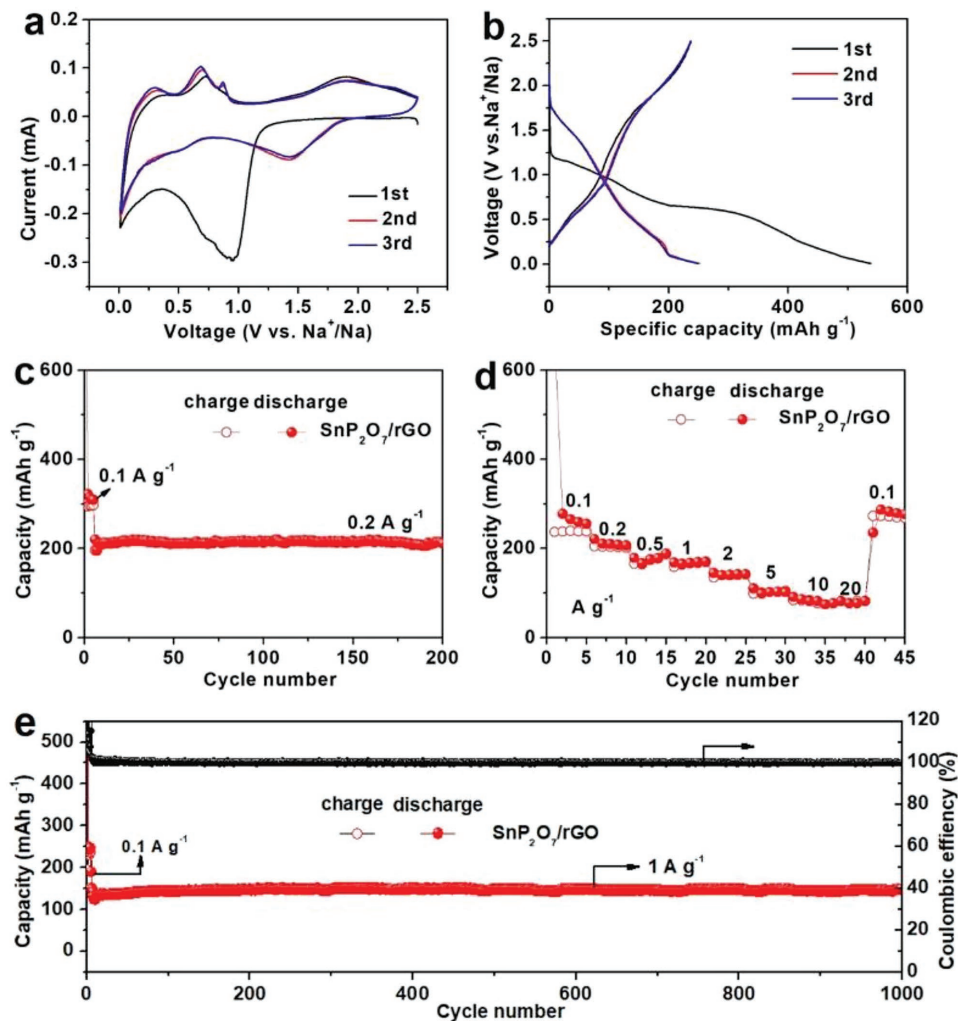


Figure 4. Electrochemical performances of SnP₂O₇/rGO. a) CV curves at a scan rate of 0.1 mV s⁻¹. b) Charge–discharge profiles at the current density of 0.1 A g⁻¹. c) Cycling performance at 0.2 A g⁻¹. d) Rate performance. e) Long-term cycling performance at 1 A g⁻¹.

This movement also renders the alloying reaction of Sn–Na to appear at 0.4 V, despite it is almost covered by the background. Meanwhile, the cathodic peak close to the discharging end is kept, confirming the good reversibility of the intercalation reaction in carbon. After that, the CV curves overlap with the previous scan, suggesting the good stability of the electrode. Figure 4b shows the discharge/charge voltage profiles of SnP₂O₇/rGO at 0.1 A g⁻¹ during the first three cycles. The first discharge/charge capacity is 538.2/237.3 mA h g⁻¹, resulting in an initial coulombic efficiency about 44.1%. The low initial coulombic efficiency is associated with the irreversible electrochemical reactions upon cycling, such as the formation of an SEI film, the reduction reaction of SnP₂O₇ and the trapping of Na⁺ in rGO (Figure S10, Supporting Information).^[41] Figure 4c shows the cycling performance of SnP₂O₇/rGO at 0.2 A g⁻¹, after electrochemical activation for the first three cycles at 0.1 A g⁻¹. This composite exhibits a stable cycling with the capacity at 213 mA h g⁻¹ and the capacity retention at 99%. This composite also presents a superior rate performance (Figure 4d), where it delivers a capacity of 254.7 mA h g⁻¹

at 0.1 A g⁻¹, 210.7 mA h g⁻¹ at 0.2 A g⁻¹, 178.5 mA h g⁻¹ at 0.5 A g⁻¹, 170.3 mA h g⁻¹ at 1 A g⁻¹, 142 mA h g⁻¹ at 2 A g⁻¹, 103 mA h g⁻¹ at 5 A g⁻¹, and 91.1 mA h g⁻¹ at 10 A g⁻¹. Encouraged by the above results, the long-term cycling of SnP₂O₇/rGO at high rates was examined. As displayed in Figure 4e, SnP₂O₇/rGO exhibits a reversible capacity of 148 mA h g⁻¹ after 1000 cycles at 1 A g⁻¹, giving a capacity retention about 99%. More importantly, there is no apparent capacity fluctuation throughout the whole process, making it great potential in the future.^[42] The voltage profiles at different cycles are similar (Figure S11, Supporting Information), confirming the good reversibility of these electrochemical reactions. But TEM images reveal that SnP₂O₇ is heavily pulverized after 1000 cycles (Figure S12, Supporting Information). Fortunately, they are still firmly attached to carbon, which makes them active in the discharging/charging processes. This result indicates that the excellent cycling stability does not come from the robust structure of SnP₂O₇, but from the strong adhesion of SnP₂O₇ on rGO that effectively keep it always active upon cycling. Meanwhile, the particle pulverization promotes the reaction

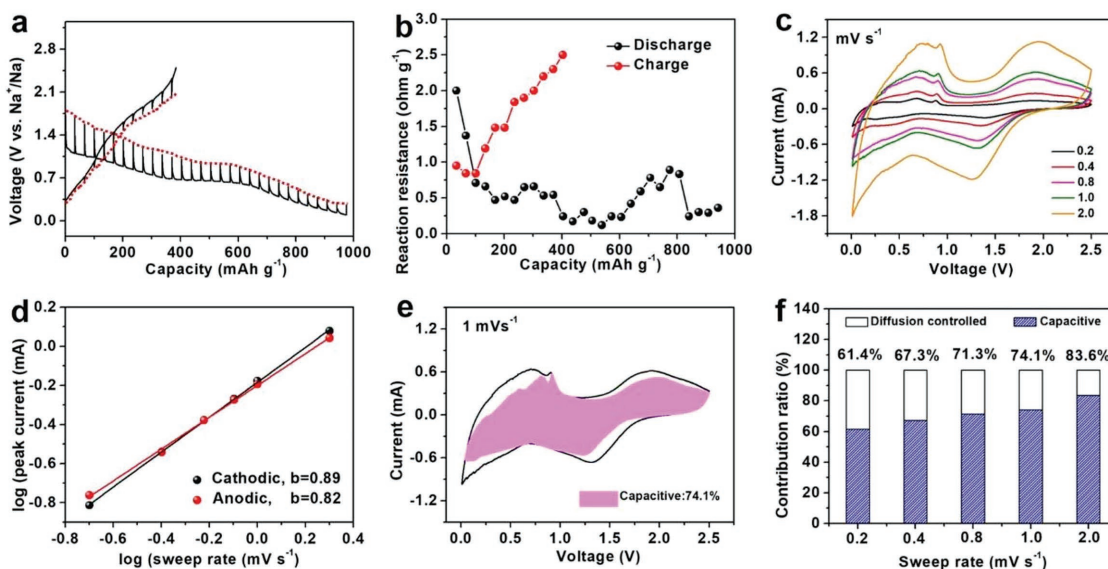


Figure 5. Kinetic analysis of electrochemical reactions in $\text{SnP}_2\text{O}_7/\text{rGO}$. a) GITT voltage profiles at the first cycle. b) Reaction resistances at the first cycle. c) CV curves at various sweep rates. d) Plots of $\log(\text{sweep rate})$ versus $\log(\text{peak current})$. e) Capacitive contribution in the CV curve obtained at 1 mV s^{-1} . f) Capacitive contribution in the CV curves obtained at different sweep rates.

kinetics, as evidenced by electrochemical impedance spectra (EIS) (Figure S13, Supporting Information). Both the surface-film resistance (R_f) and charge-transfer resistance (R_{ct}) significantly decrease after cycles. The similar cycling stability is also confirmed at other high rates. For example, $\text{SnP}_2\text{O}_7/\text{rGO}$ can present a capacity retention of 94.5 % after 500 cycles at 5 A g^{-1} , or 88.9% after 500 cycles at 8 A g^{-1} (Figure S14, Supporting Information). This excellent stability outperforms many Sn-based anode materials (Table S1, Supporting Information). All these performances were obtained with propylene carbonate (PC) as the electrolyte. If diethylene glycol dimethyl ether, a typical ether-based electrolyte, was used as the electrolyte, the cycling performance of $\text{SnP}_2\text{O}_7/\text{rGO}$ degraded fast (Figure S15, Supporting Information).

To understand the excellent electrochemical performance of $\text{SnP}_2\text{O}_7/\text{rGO}$, the galvanostatic intermittent titration technique (GITT) was used to investigate the different charge/discharge levels. As shown in Figure 5a, the dotted lines represent the quasi-equilibrium open-circuit potential (OCP). It is noted that OCP slowly but steady decreases with the state of discharge, which can be assigned to the enhanced conductivity caused by in situ formed metals or intermetallics. The opposite change occurs to the desodiation process, where the OCP gradually increases as the charging proceeds. The average reaction resistance derived from these curves is $\approx 0.5 \Omega$ for the discharging process, and $\approx 2 \Omega$ for the charging process (Figure 5b), indicating the good reaction kinetics. This conclusion is also supported by CV curves at different sweep rates. As shown in Figure 5c, the CV curves basically keep the shape and contour at different sweep rates, indicating the same electrochemical reactions. The logarithmic plot of the peak current versus sweep rate is indicative of the rate-limited characteristics by Equation (1)^[43]

$$i = av^b \quad (1)$$

where b is especially important. $b = 0.5$ implies a diffusion-controlled process, while $b = 1.0$ reflects a surface-controlled process. Usually, b locates between 0.5 and 1.0, suggesting a mixed contribution of both processes. In our case, b values of the cathodic and anodic peaks are 0.89 and 0.82 (Figure 5d), indicating the substantial contribution from a surface-controlled process. This result explains the superior rate performance of $\text{SnP}_2\text{O}_7/\text{rGO}$. The rough estimation of the two processes could be done by Equation (2)^[44]

$$i(v) = k_1v + k_2v^{1/2} \quad (2)$$

where k_1v is the contribution from surface capacitances and $k_2v^{1/2}$ is the contribution from diffusion-controlled processes. If divided both sides by $v^{1/2}$, this equation becomes Equation (3)^[45]

$$i/v^{1/2} = k_1v^{1/2} + k_2 \quad (3)$$

Here, the plot of $i/v^{1/2}$ against $v^{1/2}$ gives the specific data of k_1 and k_2 . Therefore, the contribution ratio of the two processes at a fixed potential is obtained. Using this method, we can identify the ratio of the two processes throughout the potential window. As shown in Figure 5e, the surface-controlled process contributes 74.1% of the total Na-ion storage at 1 mV s^{-1} . Moreover, this ratio increases with the increasing sweep rate (Figure 5f). At 2 mV s^{-1} , the contribution of this process to the Na-ion storage is up to 83.6%.

In view of excellent performances of $\text{SnP}_2\text{O}_7/\text{rGO}$ in half cells, it is coupled with home-made $\text{Na}_3\text{V}_2(\text{PO}_4)_3/\text{C}$ as a cathode material (Figure S16, Supporting Information) for full cells.^[46] Here, both the anode and cathode materials are composed of phosphates (Figure 6a). The full cell was cycled between 1.0 and 3.4 V at a current density of 0.5 A g^{-1} . As illustrated in Figure 6b, the full cell exhibits an average output voltage around

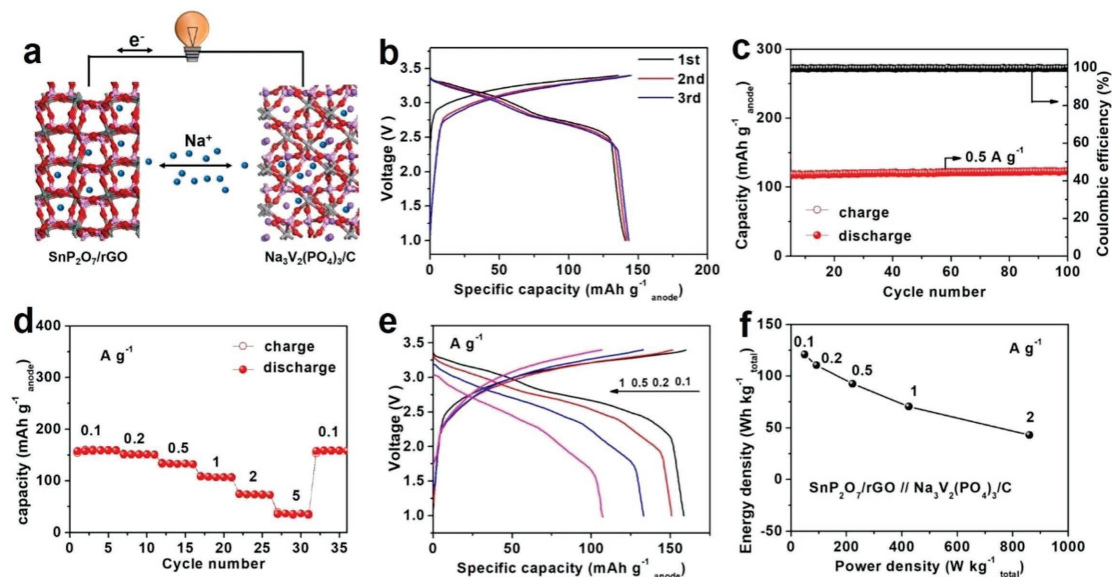


Figure 6. Electrochemical performances of the full cell ($\text{SnP}_2\text{O}_7/\text{rGO} // \text{Na}_3\text{V}_2(\text{PO}_4)_3/\text{C}$). a) Schematic illustration on electrode materials in full cells, b) discharge/charge curves at the first three cycles, c) cycling performance at 0.5 A g^{-1} except the first five cycles at 0.1 A g^{-1} , and d) rate performance. e) Discharge/charge curves at different current densities. All these capacities were calculated on the basis of the anode mass, $\text{SnP}_2\text{O}_7/\text{rGO}$. f) Ragone-like plot of full cells. Specific power/energy density was calculated on the basis of the total mass of anode and cathode, $\text{SnP}_2\text{O}_7/\text{rGO} + \text{Na}_3\text{V}_2(\text{PO}_4)_3/\text{C}$.

2.75 V, much higher than many reported works (Table S2, Supporting Information).^[47] The high output voltage would promote its performances in high-power cases. Meanwhile, the overpotential between discharging/charging profiles is about $\approx 0.3 \text{ V}$, reflecting the good reaction kinetics. Figure 6c presents the cycling performance of the full cell at 0.5 A g^{-1} , which keeps the specific capacity at 123 mA h g^{-1} after 100 cycles. Like the results in half cells, the capacity retention is very high, $\approx 99\%$. In the rate performance (Figure 6d), this full cell displays a capacity of $158.2 \text{ mA h g}^{-1}$ at 0.1 A g^{-1} , $150.8 \text{ mA h g}^{-1}$ at 0.2 A g^{-1} , 133 mA h g^{-1} at 0.5 A g^{-1} , $107.4 \text{ mA h g}^{-1}$ at 1 A g^{-1} , 74.3 mA h g^{-1} at 2 A g^{-1} , and 36.5 mA h g^{-1} at 5 A g^{-1} . All these capacities are obtained on the basis of the mass of the anode material. The overpotential gradually increases with the increasing current densities (Figure 6e). If we evaluate the performances of full cells in another way, it is found that it could deliver an energy density of $120.8 \text{ Wh kg}^{-1}_{\text{total}}$ at $0.049 \text{ kW kg}^{-1}_{\text{total}}$ (Figure 6f). Even if the powder density increases to $0.86 \text{ kW kg}^{-1}_{\text{total}}$, the energy density is still $43 \text{ Wh kg}^{-1}_{\text{total}}$.

3. Conclusions

In summary, $\text{SnP}_2\text{O}_7/\text{rGO}$, where SnP_2O_7 is firmly attached to rGO, was successfully prepared by a simple process. Ex situ HRTEM images and SAED patterns confirm that its electrochemical activity originates from the reversible conversion reaction between Sn and SnP_2O_7 and the alloying reaction between Sn and Na_xSn . The close contact between rGO and SnP_2O_7 keeps SnP_2O_7 attached to rGO even after the particle pulverization and enhances the charge transportation during the discharge/charge processes. Thus, $\text{SnP}_2\text{O}_7/\text{rGO}$ exhibits an extraordinarily high cycling stability, 99% of the capacity

retention after 200 cycles at 0.2 A g^{-1} , or 99% after 1000 cycles at 1 A g^{-1} . The same feature is also achieved in full cells, by $\text{SnP}_2\text{O}_7/\text{rGO}$ paired with $\text{Na}_3\text{V}_2(\text{PO}_4)_3/\text{C}$. This full cell exports an average voltage about 2.75 V, and a capacity retention about 99% after 100 cycles at 0.5 A g^{-1} . These results are quite good for a new electrode material, indicating the promising potential of metal pyrophosphates in SIBs.

4. Experimental Section

Material Synthesis: First, GO was obtained by using a modified Hummer's method.^[48] Then, 60 mg GO was dispersed in 40 mL of ethylene glycol by ultrasound. After half an hour, 350 mg of $\text{SnCl}_4 \cdot 5\text{H}_2\text{O}$ and 230 mg of $\text{NH}_4\text{H}_2\text{PO}_4$ were added under vigorous stirring at 70°C . The resultant suspension was transferred into a Teflon-lined stainless-steel autoclave with a capacity of 60 mL. After 4 h at 160°C , the product was collected by centrifugation, washed with deionized water and absolute ethanol, afterward dried under vacuum at 60°C overnight. Finally, the powders were annealed at 550°C for 6 h in Ar/H_2 (vol = 95:5%), resulting in $\text{SnP}_2\text{O}_7/\text{rGO}$.

Materials Characterization: XRD patterns were recorded on an X-ray diffractometer (Bruker D8 Advanced, Germany), with monochromatic $\text{Cu K}\alpha$ as the radiation source ($\lambda = 1.5418 \text{ \AA}$). SEM images were obtained from a field-emission scanning electron microscope (FESEM SU8010, Japan). TEM images, HRTEM images, HAADF-STEM images, and element maps were acquired by an aberration-corrected microscope (FEI Titan Themis G2 300, USA) operated at an accelerating voltage of 300 kV with a beam current of 80 pA, a convergence semi-angle of 21 mrad, and a collection semi-angle snap in the range of 80–379 mrad. Ex situ SAED was conducted on a field-emission transmission electron microscope (FEI Tecnai F20, USA) at 200 kV equipped with an OneView IS (Gatan) camera with the frame rates up to 300 fps. XPS were achieved by an X-ray photoelectron spectrometer (ESCALAB 250, Thermo Scientific, USA). Raman spectra came from a micro-Raman spectrometer (HORIBA JY LabRAM H800, Japan), using an excitation at 632 nm at room temperature. N_2 sorption isotherms were recorded on a

physiosorption analyzer (Micromeritics ASAP 2020 HD88, USA) at 77 K. TGA was taken from a Mettler Toledo TGA/SDTA 851 thermal analyzer from room temperature to 800 °C in air.

Electrochemical Measurements: Electrochemical performances of SnP₂O₇/rGO as an anode material for SIBs were examined using CR2032-type coin cells, where the working electrode was made of SnP₂O₇/rGO, acetylene black, and carboxy methyl cellulose in a weight ratio of 7:2:1 on a copper foil. These materials were milled by hands for half an hour with droplets of H₂O, giving a black but sticky slurry. This slurry was spread on a clean copper foil by a doctor blade. After dried in vacuum at 60 °C for 12 h, the foil was cut into small discs with a diameter of 12 mm. The mass loading of SnP₂O₇/rGO on the discs is about 1.5 mg cm⁻². Then, the working electrode was assembled with sodium metal as a counter electrode, Whatman glass microfiber filters (Whatman GF/F) as a separator, and 1.0 M NaClO₄ in PC containing 3 wt% fluoroethylene carbonate as an electrolyte in an Ar-filled groove box (Mikrouna, Super 1220/750/900, H₂O < 1 ppm; O₂ < 1 ppm). Galvanostatic discharge/charge profiles and GITT measurements were performed on battery cyclers (LAND CT-2001A, China) between 0.01 and 2.5 V at 25 °C. CVs were measured on an electrochemical workstation (CHI 760E, China) at room temperature. EIS were obtained from an electrochemical workstation (Autolab PGSTAT 302N) in a frequency range of 100 KHz to 0.01 Hz. In full cells, the anode was made by the above protocol and then electrochemically activated for five cycles to eliminate the capacity loss of the full cells in the first cycle. The cathode was fabricated by homemade Na₃V₂(PO₄)₃/C, acetylene black and poly(vinylidene fluoride) in a weight ratio of 8:1:1 on an aluminum foil. The capacity ratio between the cathode and anode was controlled at 1:1.2. The anode capacity slightly exceeds the cathode capacity, promoting the utilization of cathode materials and preventing the formation of dendrites.

Supporting Information

Supporting Information is available from the Wiley Online Library or from the author.

Acknowledgements

The authors want to thank the financial support from National Nature Science Foundation of China (Nos. 21471090, 61527809, 51172076, 51502007, and 51672007), Taishan Scholarship in Shandong Provinces (No. ts201511004), and the Fundamental Research Funds of Shandong University (2018JC023).

Conflict of Interest

The authors declare no conflict of interest.

Keywords

anodes, full cells, phosphates, sodium-ion batteries

Received: July 8, 2018

Revised: August 12, 2018

Published online: September 11, 2018

- [1] H. G. Wang, S. Yuan, D. L. Ma, X. B. Zhang, J. M. Yan, *Energy Environ. Sci.* **2015**, *8*, 1660.
[2] L. D. Lin, X. N. Xu, C. X. Chu, M. K. Majeed, J. Yang, *Angew. Chem., Int. Ed. Engl.* **2016**, *55*, 14063.

- [3] X. L. Huang, R. Z. Wang, D. Xu, Z. L. Wang, H. G. Wang, J. J. Xu, Z. Wu, Q. C. Liu, Y. Zhang, X. B. Zhang, *Adv. Funct. Mater.* **2013**, *23*, 4345.
[4] W. Li, F. Wang, S. S. Feng, J. X. Wang, Z. K. Sun, B. Li, Y. H. Li, J. P. Yang, A. A. Elzatahry, Y. Y. Yao, D. Y. Zhao, *J. Am. Chem. Soc.* **2013**, *135*, 18300.
[5] Z. L. Wang, D. Xu, H. G. Wang, Z. Wu, X. B. Zhang, *ACS Nano* **2013**, *7*, 2422.
[6] J. Liu, K. P. Song, P. A. V. Aken, J. Maie, Y. Yu, *Nano Lett.* **2014**, *14*, 2597.
[7] D. L. Ma, H. G. Wang, Y. Li, D. Xu, S. Yuan, X. L. Huang, X. B. Zhang, Y. Zhang, *Nano Energy* **2014**, *10*, 295.
[8] P. V. Prikhodchenko, J. Gun, S. Sladkevich, A. A. Mikhaylov, O. Lev, Y. Y. Tay, S. K. Batabyal, D. Y. W. Yu, *Chem. Mater.* **2012**, *24*, 4750.
[9] S. Yuan, Y. B. Liu, D. Xu, D. L. Ma, S. Wang, X. H. Yang, Z. Y. Cao, X. B. Zhang, *Adv. Sci.* **2015**, *2*, 1400018.
[10] Q. M. Tang, Y. H. Cui, J. W. Wu, D. Y. Qu, A. P. Baker, Y. H. Ma, X. N. Song, Y. C. Liu, *Nano Energy* **2017**, *41*, 377.
[11] A. Darwiche, C. Marino, M. T. Sougrati, B. Fraisse, L. Stievano, L. Monconduit, *J. Am. Chem. Soc.* **2012**, *134*, 20805.
[12] S. Liu, J. K. Feng, X. F. Bian, J. Liu, H. Xu, *Energy Environ. Sci.* **2016**, *9*, 1229.
[13] X. Liu, K. Zhang, K. X. Lei, F. J. Li, Z. L. Tao, J. Chen, *Nano Res.* **2016**, *9*, 198.
[14] M. Wang, Z. Z. Yang, W. H. Li, L. Gu, Y. Yu, *Small* **2016**, *12*, 2559.
[15] X. J. Zhang, G. Zhu, M. Wang, J. B. Li, T. Lu, L. K. Pan, *Carbon* **2017**, *116*, 686.
[16] K. Zhang, Z. Hu, X. Liu, Z. L. Tao, J. Chen, *Adv. Mater.* **2015**, *27*, 3305.
[17] X. N. Li, J. W. Liang, Z. G. Hou, W. Q. Zhang, Y. Wang, Y. C. Zhu, Y. T. Qian, *Adv. Funct. Mater.* **2015**, *25*, 5229.
[18] H. Wang, X. Z. Lan, D. L. Jiang, Y. Zhang, H. H. Zhong, Z. P. Zhang, Y. Jiang, *J. Power Sources* **2015**, *283*, 187.
[19] J. F. Qian, Y. Xiong, Y. L. Cao, X. P. Ai, H. X. Yang, *Nano Lett.* **2014**, *14*, 1865.
[20] F. Wan, J. Z. Guo, X. H. Zhang, J. P. Zhang, H. Z. Sun, Q. Y. Yan, D. X. Han, L. Niu, X. L. Wu, *ACS Appl. Mater. Interface* **2016**, *8*, 7790.
[21] J. X. Song, Z. X. Yu, M. L. Gordin, X. L. Li, H. S. Peng, D. H. Wang, *ACS Nano* **2015**, *9*, 11933.
[22] J. Pan, N. N. Wang, Y. L. Zhou, X. F. Yang, W. Y. Zhou, Y. T. Qian, J. Yang, *Nano Res.* **2017**, *10*, 1794.
[23] H. J. Ying, W. Q. Han, *Adv. Sci.* **2017**, *4*, 1700298.
[24] B. Zhang, G. Rousse, D. Folx, R. Dugas, D. A. D. Corte, J. M. Tarascon, *Adv. Mater.* **2016**, *28*, 9824.
[25] Y. H. Liu, Y. H. Xu, Y. J. Zhu, J. N. Culver, C. A. Lundgren, K. Xu, C. S. Wang, *ACS Nano* **2013**, *7*, 3627.
[26] M. H. Wang, H. Yang, X. L. Zhou, W. Shi, Z. Zhou, P. Cheng, *Chem. Commun.* **2016**, *52*, 717.
[27] W. H. Wang, L. Shi, D. Lan, Q. Li, *J. Power Sources* **2018**, *377*, 1.
[28] S. Yuan, Y. H. Zhu, W. Li, S. Wang, D. Xu, L. Li, Y. Zhang, X. B. Zhang, *Adv. Mater.* **2017**, *29*, 1602469.
[29] X. Yang, R. Y. Zhang, J. Zhao, Z. X. Wei, D. X. Wang, X. F. Bie, Y. Gao, J. Wang, F. Du, G. Chen, *Adv. Energy Mater.* **2017**, *8*, 1701827.
[30] I. Bezza, V. Trouillet, A. Fiedler, M. Bruns, S. Indris, H. Ehrenberg, I. Saadoun, *Electrochim. Acta* **2017**, *252*, 446.
[31] R. F. Nie, J. J. Shi, W. C. Du, W. S. Ning, Z. Y. Hou, F. S. Xiao, *J. Mater. Chem. A* **2013**, *1*, 9037.
[32] J. F. Mao, X. L. Fan, C. Luo, C. S. Wang, *ACS Appl. Mater. Interface* **2016**, *8*, 7147.
[33] X. H. Xiong, C. H. Yang, G. H. Wang, Y. W. Lin, X. Ou, J. H. Wang, B. T. Zhao, M. L. Liu, Z. Lin, K. W. Huang, *Energy Environ. Sci.* **2017**, *10*, 1757.

- [34] C. Zhang, X. Wang, Q. F. Liang, X. Z. Liu, Q. H. Weng, J. W. Liu, Y. J. Yang, Z. H. Dai, K. J. Ding, Y. Bando, J. Tang, *Nano Lett.* **2016**, *16*, 2054.
- [35] J. Liu, P. Kopold, C. Wu, P. A. van Aken, J. Maier, Y. Yu, *Energy Environ. Sci.* **2015**, *8*, 3531.
- [36] Y. Li, J. Li, *J. Phys. Chem. C* **2008**, *112*, 14216.
- [37] Y. Zheng, T. F. Zhou, C. F. Zhang, J. F. Mao, H. K. Liu, Z. P. Guo, *Angew. Chem., Int. Ed. Engl.* **2016**, *55*, 3408.
- [38] L. B. Zhang, H. B. Wu, B. Liu, X. W. Lou, *Energy Environ. Sci.* **2014**, *7*, 1013.
- [39] F. A. Soto, P. F. Yan, M.-H. Engelhard, A. Marzouk, C. M. Wang, G. L. Xu, Z. H. Chen, K. Amine, J. Liu, V. L. Sprenkle, F. El-Mellouhi, P. B. Balbuena, X. L. Li, *Adv. Mater.* **2017**, *29*, 1606860.
- [40] T. F. Wu, G. L. Dai, C. C. Qin, J. L. Cao, Y. F. Tang, Y. F. Chen, *Ionics* **2016**, *22*, 2315.
- [41] T. S. Wang, P. Hu, C. J. Zhang, H. P. Du, Z. H. Zhang, X. G. S. G. Chen, J. W. Xiong, G. L. Cui, *ACS Appl. Mater. Interface* **2016**, *8*, 7811.
- [42] A. R. Park, C. M. Park, *ACS Nano* **2017**, *11*, 6074.
- [43] S. H. Choi, Y. C. Kang, *Nano Res.* **2015**, *8*, 1595.
- [44] S. X. Deng, J. W. Li, S. B. Sun, H. Wang, J. B. Liu, H. Yan, *Electrochim. Acta* **2014**, *146*, 37.
- [45] T. Brezesinski, J. Wang, J. Polleux, B. Dunn, S. H. Tolbert, *J. Am. Chem. Soc.* **2009**, *131*, 1802.
- [46] G. Q. Li, D. L. Jiang, H. Wang, X. Z. Lan, H. H. Zhong, Y. Jiang, *J. Power Sources* **2014**, *265*, 325.
- [47] F. E. Niu, J. Yang, N. N. Wang, D. P. Zhang, W. L. Fan, J. Yang, Y. T. Qian, *Adv. Funct. Mater.* **2017**, *27*, 1700522.
- [48] W. Hummers, R. Offeman, *J. Am. Chem. Soc.* **1958**, *80*, 1339.